



HAL
open science

Multi-scale three-dimensional analysis on local arrestability of intergranular crack in high-strength martensitic steel

Akinobu Shibata, Ivan Gutierrez-Urrutia, Akiko Nakamura, Goro Miyamoto, Yazid Madi, Jacques Besson, Toru Hara, Kaneaki Tsuzaki

► **To cite this version:**

Akinobu Shibata, Ivan Gutierrez-Urrutia, Akiko Nakamura, Goro Miyamoto, Yazid Madi, et al.. Multi-scale three-dimensional analysis on local arrestability of intergranular crack in high-strength martensitic steel. *Acta Materialia*, 2022, 234, pp.118053. 10.1016/j.actamat.2022.118053. hal-03799344

HAL Id: hal-03799344

<https://hal.science/hal-03799344>

Submitted on 5 Oct 2022

HAL is a multi-disciplinary open access archive for the deposit and dissemination of scientific research documents, whether they are published or not. The documents may come from teaching and research institutions in France or abroad, or from public or private research centers.

L'archive ouverte pluridisciplinaire **HAL**, est destinée au dépôt et à la diffusion de documents scientifiques de niveau recherche, publiés ou non, émanant des établissements d'enseignement et de recherche français ou étrangers, des laboratoires publics ou privés.



Multi-scale three-dimensional analysis on local arrestability of intergranular crack in high-strength martensitic steel

Akinobu Shibata^{a,b,c,*}, Ivan Gutierrez-Urrutia^a, Akiko Nakamura^a, Goro Miyamoto^{a,d}, Yazid Madi^e, Jacques Besson^e, Toru Hara^a, Kaneaki Tsuzaki^{a,b,d}

^a Research Center for Structural Materials, National Institute for Materials Science (NIMS), 1-2-1, Sengen, Tsukuba, 305-0047, Japan

^b Elements Strategy Initiative for Structural Materials (ESISM), Kyoto University, Yoshida-honmachi, Sakyo-ku, Kyoto, 606-8501, Japan

^c PRESTO, Japan Science and Technology Agency, 4-1-8 Honcho, Kawaguchi, Saitama, 332-0012, Japan

^d Institute for Materials Research, Tohoku University, Aoba-ku, Sendai, 980-8577, Japan

^e Centre des Matériaux, MINES ParisTech, CNRS UMR 7633, BP 87, 91003, Evry, France

ARTICLE INFO

Article history:

Received 26 December 2021

Revised 12 April 2022

Accepted 19 May 2022

Available online 21 May 2022

Keywords:

Intergranular failure

Local crack-arrestability

Martensite

X-ray computed tomography

Serial sectioning

Electron backscatter diffraction (EBSD)

ABSTRACT

The present study investigated the local arrestability of intergranular crack in high-strength martensitic steel through multi-scale three-dimensional (3D) analysis using X-ray computed tomography and focused ion beam machining (FIB)-scanning electron microscopy (SEM) serial sectioning combined with electron backscattering diffraction (3D EBSD). Macroscopic analysis using X-ray computed tomography demonstrated discontinuous propagation of the intergranular cracks, indicating local arrest of the crack propagation. An analysis of the opening displacement of each crack component revealed that the resolved normal stress was not the only factor determining the intergranular crack propagation path. The relationship between the microstructure and local crack-arrestability was microscopically analyzed using FIB-SEM serial sectioning. The 3D EBSD analysis clearly suggested that the crack propagations were arrested at the low-angle grain boundary plane segments and at the grain boundary triple junctions surrounded by relatively large martensite variants. Moreover, the larger martensite variants around grain boundaries contributed to the plastic accommodation of stress concentration and promoted crack-tip blunting. We propose that increasing the fraction of low-angle grain boundary plane segments as well as that of large martensite variants existing around grain boundaries can enhance local crack-arrestability and retard intergranular fracture of high-strength martensitic steels.

© 2022 The Author(s). Published by Elsevier Ltd on behalf of Acta Materialia Inc.

This is an open access article under the CC BY license (<http://creativecommons.org/licenses/by/4.0/>)

1. Introduction

To establish secure and robust infrastructure in various industrial and social environments, it is necessary to develop novel materials with enhanced strength and reliability. Although high strength is relatively easy to achieve, brittle premature fracture hinders the wide application of high-strength materials (e.g., steels with a tensile strength of 1.5 GPa class). The most widely used approach for designing materials with reasonable toughness entails sacrificing strength to a certain extent. The key to prevent brittle fracture and improve the toughness of metallic materials is to understand the relationship between the fracture behavior and microstructure.

The typical brittle fracture modes in metals and alloys are classified into transgranular and intergranular fractures [1]. Intergranu-

lar fractures are often linked with significantly more severe brittle behaviors. “Grain boundary engineering” has been developed as a methodology to improve the bulk properties and performances of materials based on the known properties of grain boundaries and interfaces [2]. One of the main aims of grain boundary engineering is to retard intergranular fractures through microstructure control. Watanabe and Tsurekawa [3] demonstrated the importance of introducing low- Σ coincidence boundaries and/or reducing random boundaries for controlling the intergranular fractures in intrinsically brittle materials, such as refractory metal molybdenum and intermetallic Ni₃Al. Bechtel et al. [4] successfully improved the susceptibility of nickel alloys to hydrogen embrittlement by increasing the fraction of low-energy grain boundaries, such as annealing twin boundaries. Bachurin [5] studied the intergranular fracture of nanocrystalline palladium by atomistic simulations and proposed that low-angle grain boundaries of both general and special character could act as obstacles to intergranular fracture. In addition to these works, several studies have reported that controlling the

* Corresponding author.

E-mail address: SHIBATA.Akinobu@nims.go.jp (A. Shibata).

grain boundary character can retard intergranular fracture [6–9]. However, to date, both the atomistic simulations and the experimental approaches described above have been limited to materials with relatively simple microstructures.

The most commercially used structural metallic materials are iron and steel. Martensitic phase transformation, which is diffusionless and displacive in nature, has always been a key factor for controlling the microstructure of high-strength steels. Intergranular fractures, particularly hydrogen embrittlement [10,11] or segregation-induced embrittlement [12,13], often occur in high-strength martensitic steels. Therefore, improving the resistance of martensitic structures to intergranular fracture is an urgent issue for realizing advanced high-strength steels. The martensite in low- and medium-carbon steels, namely, lath martensite, exhibits a complicated microstructure and comprises several structural units with different size scales: lath, block, packet, and prior austenite grain [14–17]. A lath is a unit corresponding to a single martensite crystal with a thickness of approximately 0.2 μm and contains a high density of dislocations ($\sim 10^{15} \text{ m}^{-2}$ [18]). The boundaries between laths are low-angle boundaries, whose misorientation angle is usually less than 3° [17]. A block corresponds to a single crystallographic martensite variant, which is composed of an aggregation of laths with nearly the same crystallographic orientation. A packet consists of laths with nearly the same habit plane orientation or parallel plane relationship with respect to the parent austenite phase. A prior austenite grain corresponds to a single grain in the parent austenite state before the transformation. The martensite structure contains several types of high-angle boundaries, namely, block boundaries and packet boundaries, in addition to prior austenite grain boundaries. Intergranular fractures mainly occur along the prior austenite grain boundaries [19], though several papers reported the intergranular cracking on lath boundaries or block boundaries [20–23]. Several martensite variants nucleate at the original austenite grain boundary by transformation [24–26], and the growth of martensite variants occasionally stops at the austenite grain boundaries. Accordingly, a given austenite grain boundary is divided into several segments sharing the same spatial boundary plane, which exhibit different crystallographic features (for example, misorientation angle). In other words, the prior austenite grain boundary is different from a conventional uniform grain boundary in polycrystalline materials, but exhibits an inhomogeneous structure from a crystallographic point of view. For conventional polycrystalline materials, the grain boundary character changes when the crack reaches a grain boundary triple junction, while the character changes during crack propagation along a prior austenite grain boundary plane in the lath martensite structure. However, to best of our knowledge, there have been no reports concerning the effect of the complicated structure of the prior austenite grain boundary on the intergranular fracture behavior. On this basis, the intergranular fracture behavior of martensitic steels remains an extremely complicated subject and elucidating the underlying mechanism is an important scientific and engineering challenge.

Crack morphology is an important characteristic of intergranular fractures; the crack surface area, crack discontinuity, and crack arrestability are closely related to the macroscopic mechanical properties. Although conventional two-dimensional (2D) surface observation is appropriate for statistical analysis, it has some inevitable limitations for analyzing the intergranular crack propagation behavior. For example, quantitative analysis of the crack morphology is impossible. Moreover, boundary orientation is difficult to identify, although it is closely related to the resolved stress state and the resulting driving force for crack propagation. Several studies have demonstrated that non-destructive X-ray computed tomography using transmitted images is a useful method for analyzing the macroscopic three-dimensional (3D) crack morphology and

distribution of defects (scale: $\mu\text{m}^3\text{--mm}^3$) [27–31]. The combination of serial sectioning and electron backscattering diffraction (EBSD) analysis allows for 3D microstructural/crystallographic characterization on a microscopic scale (scale: $\text{nm}^3\text{--}\mu\text{m}^3$) [32–35]. In particular, the 3D EBSD technique can analyze the relationship between the local crack-arrestability and microstructure in detail. Therefore, 3D observation with different scales is a promising method for deeply understanding the fundamental aspects of intergranular crack propagation. In this regard, a multi-scale 3D analysis on the local arrestability behavior of intergranular crack propagation in a high-strength as-quenched martensitic steel was conducted in this study and an appropriate martensite microstructure for retarding intergranular fracture was proposed.

2. Experimental procedure

The material used in the present study was an Fe-8Ni-0.1C alloy with a high nickel content to obtain high hardenability. The chemical composition of the material (in mass%) is C: 0.116, Si: 0.005, Mn: 0.01, P: 0.001, S:0.0015, Al: 0.033, Ni: 7.94, and Fe: balance. The as-received steel plates were austenitized at 1000°C for 30 min, followed by ice-brine quenching and sub-zero cooling in liquid nitrogen. The 0.2% proof strength and tensile strength of the heat-treated specimen evaluated by the tensile tests were 920 and 1191 MPa, respectively [36]. Compact tension specimens with a thickness of 12.5 mm (B) and a width of 25 mm (W) were cut from the heat-treated steel plates via spark wire cutting. After introducing fatigue pre-cracks with lengths ranging from 0.45 to 0.55 W , side grooves were machined to the pre-cracked specimens (the thickness at the root of the side grooves (B_N) was 10 mm). Unloading compliance tests were performed to obtain the $J - \Delta a$ resistance curves. J is the J-integral value obtained from $J = J_{el} + J_{pl}$; J_{el} was computed using linear elastic fracture mechanics, and J_{pl} was incrementally computed using the plastic area under the load – displacement curve. Δa is the crack extension length evaluated in accordance with the single-specimen test method of the ASTM E1820-17 standard [37]. Unload/reload sequences were performed for a displacement interval of 0.025 mm. The rate of load-line displacement for the test was set at $2.5 \times 10^{-5} \text{ mm s}^{-1}$, and the corresponding initial rate of the stress intensity factor was $8.5 \times 10^{-3} \text{ MPa m}^{1/2} \text{ s}^{-1}$ (for $a_0 / W = 0.5$), indicating that the test was quasi-static. The details of the specimen fabrication and mechanical testing are described in [36].

Conventional 2D observations on the fracture surface and crack propagation were performed using scanning electron microscopy (SEM, ZEISS: Sigma and JEOL: JSM-7800F). The macroscopic 3D crack propagation morphologies were analyzed by computed tomography using X-ray microscopy (ZEISS: Xradia 620 Versa). A specimen with the dimensions of $\sim 2 \text{ mm}$ (W) \times 16 mm (L) \times 1 mm (T) was cut from the mid-thickness region of the tested compact tension specimen by spark wire cutting. Absorption contrast images were acquired around a 360° rotation of the specimen in steps of 0.1° using a flat panel extension sensor and optical magnification lenses ($\times 4$ and $\times 20$) with a tube voltage of 80 and 100 kV. The images were processed using the ORS Dragonfly Pro software. For microscopic analysis, a pillar with the dimensions of $\sim 25 \mu\text{m} \times 25 \mu\text{m} \times 25 \mu\text{m}$ containing cracks was fabricated from the tested compact tension specimen using a focused ion beam (FIB, ThermoFisher Scientific: Scios2) with an acceleration voltage of 30 kV. The 3D crack propagation behavior was analyzed by serial sectioning using an orthogonal FIB-SEM system (Hitachi High-Tech: SMF-1000) [38], which realizes so-called “static set-up [33]” for 3D EBSD. The specimen was milled with an interval of 100 nm using a Ga^+ beam with an accelerating voltage of 30 kV and a beam current of 13 nA. Microstructural observation and crystallographic orientation mapping on every milled surface were conducted using an

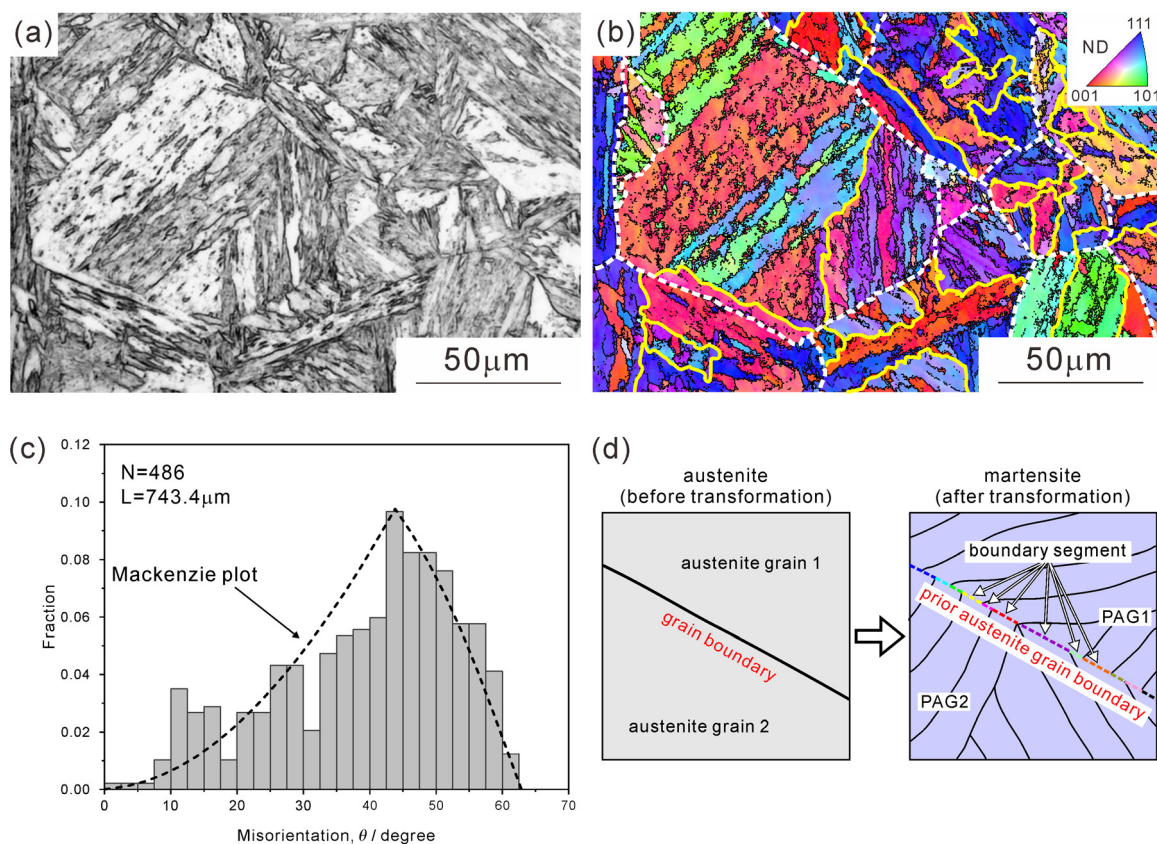


Fig. 1. (a) Optical microscopy image of the as-quenched martensite and (b) EBSD orientation map of the same area as (a), where the positions of the block boundaries, packet boundaries, and prior austenite grain boundaries are indicated by the black, yellow, and white broken lines, respectively. (c) Misorientation profile of the prior austenite grain boundaries. The data was obtained from eight different prior austenite grain boundaries (segment number: 486 and total length: 743.4 μm). The superimposed Mackenzie plot [40] represents the theoretical misorientation distribution of a polycrystal with random orientation. (d) Schematic of a prior austenite grain boundary.

in-lens secondary electron detector and an EBSD system, respectively. The EBSD measurements were performed using high speed Hikari camera with a step size of 100 nm at an acceleration voltage of 20 kV (TSL: OIM Data Collection program). The specimen was tilted 70° with respect to the incident electron beam direction to obtain the EBSD Kikuchi diffraction patterns. The SEM images were taken under the same geometry so that the images were modified considering a tilting angle of 70°. The open-source software DREAM.3D [39] was used to reconstruct the 3D EBSD orientation maps. Voxels with a low image quality (<120) or confidence index (<0.1) were not considered. Centroid- and misorientation-based algorithms were used to correct the sub-pixel misalignment between the 2D sections. The individual grains were defined by voxels with a misorientation of < 5° with respect to their six face-sharing neighbors. The reconstructed 3D EBSD orientation maps were analyzed using the open-source software ParaView. In the following sections, the specimen coordinate system is set as: X is the macroscopic tensile axis, -Y is the macroscopic crack propagation direction, and Z is the depth direction across the observed section in FIB-SEM serial sectioning (Z = 0 means the first section).

3. Results

3.1. Mechanical properties and 2D analysis of crack propagation

Fig. 1 shows (a) an optical microscopy image and (b) an EBSD orientation map of the heat-treated specimen, where the positions of the block boundaries, packet boundaries, and prior austenite grain boundaries are indicated by the black, yellow, and white broken lines, respectively. The boundary positions were deter-

mined by crystallographic variant analysis using EBSD orientation data [16,17]. Each block and packet boundaries correspond to the boundaries between specific martensite variants, whereas the prior austenite grain boundaries are different from inter-variant boundaries. Therefore, we can correctly distinguish these boundaries. The microstructure was identified as a typical lath martensite structure as several blocks and packets can be observed inside the prior austenite grains. We chose eight different prior austenite grain boundaries (total boundary length: 743.4 μm) in the low magnification EBSD orientation map (image is not shown) and examined the misorientation of each boundary segment. The misorientation profile of the prior austenite grain boundaries is presented in Fig. 1(c). We can find that the eight grain boundaries in the parent austenite state were divided into 486 segments (i.e., average segment length: 1.53 μm), which exhibited different crystallographic features, due to martensitic transformation. This indicates the inhomogeneity of the prior austenite grain boundaries, where each segment divided by the intersections between the different martensite variants possessed different crystallographic features (Fig. 1(d)). The fraction corresponding to the low-angle boundary segments of the prior austenite grain boundaries (misorientation (θ) $\leq 15^\circ$) was slightly higher compared with that in the Mackenzie plot, which represents the theoretical misorientation distribution of a polycrystal with random orientation [40]. This could be attributed to the variant selection at the austenite grain boundaries during the nucleation stage of the martensitic transformation. Because prior austenite grain boundaries play the most important role for intergranular fracture in martensitic steels [19], hereafter the term “grain boundary” denotes prior austenite grain boundary, unless otherwise specified. In our previous study we confirmed

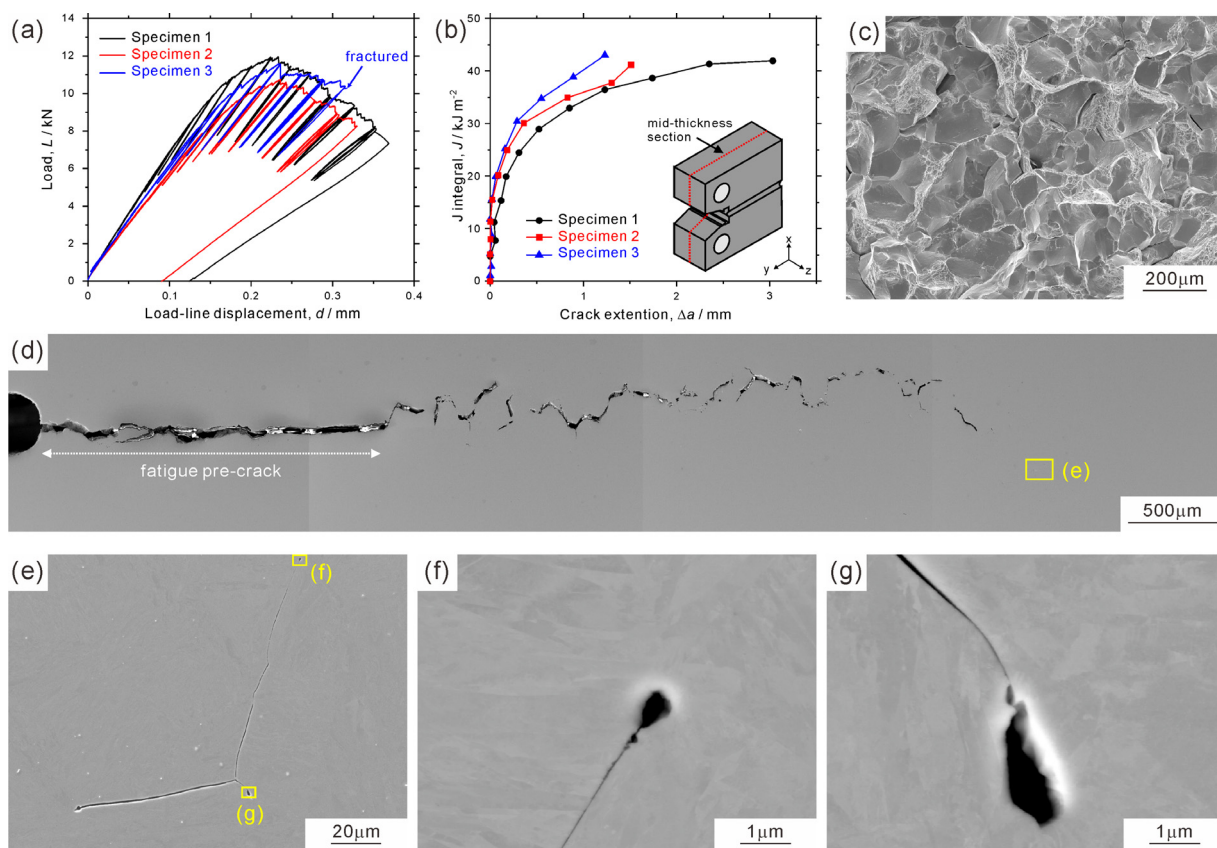


Fig. 2. (a) Load – load-line displacement curves of the unloading compliance tests, (b) $J - \Delta a$ resistance curves computed from (a), (c) SEM image showing the fracture surface after the unloading compliance test, (d, e) low magnification SEM images showing the crack propagation behavior (the observed area of (e) is indicated in (d)), and (f, g) high magnification SEM images corresponding to the areas indicated in (e). In (a, b), a part of the data from our previous paper [36] was reused with permission from Elsevier.

that the intergranular fracture in the present martensitic steel occurred on the prior austenite grain boundaries [36].

The load – load-line displacement curves of the unloading compliance test and the $J - \Delta a$ resistance curves are presented in Fig. 2(a, b) (a part of the data from our previous paper [36] was reused). We found that crack growth proceeded with finite and positive $dJ / d\Delta a$ values (here, $dJ / d\Delta a$ represents crack-growth resistance), which indicated a stable crack propagation, because the additional strain energy supplied by the external load was necessary for further crack extension [41]. Therefore, the $J - \Delta a$ resistance curves (Fig. 2(b)) revealed that the crack propagated in a stable manner, despite the brittle intergranular mode (Fig. 2(c)). The macroscopic crack propagation at the mid-thickness section was observed by SEM (Fig. 2(d-g)), where the crack propagation direction was from left to right. The existence of numerous un-cracked ligaments (un-cracked grain boundary length) implied that the crack propagation was discontinuous, at least in the observed section. Moreover, the crack tips were blunted, as shown in Fig. 2(e-g). It should be noted that the blunting behavior of the crack tip in Fig. 2(e-g) differed from that of the conventional one. In general, when blunting occurs, the opening displacement at the crack tip is smaller than that in the crack-wake region. However, the blunted crack tips shown in Fig. 2(f, g) exhibited a much larger opening displacement compared with the crack-wake region. This could be attributed to crack closure after unloading. The average opening displacement of the blunted crack-tip was 566 nm [42]. Generally, blunting is associated with the plastic accommodation at the crack tip. The notably large blunting in the present specimen indicates that the degree of plastic accommodation depended on the location along the grain boundary.

3.2. Macroscopic 3D analysis of crack propagation

The macroscopic 3D crack propagation morphologies reconstructed by X-ray computed tomography are presented in Fig. 3(a-c); (a) the entire length of the intergranular crack (including the fatigue pre-crack region) and (b, c) around the crack tip. The detailed morphology can be confirmed in supplementary material of this paper (Movie 1). The white arrows in each figure indicate the specimen coordinate system and the length corresponds to the denoted value (for example, the length of each arrow in Fig. 3(a) is 500 μm). The macroscopic directions of the crack propagation and the tensile axis were - Y direction and $\pm X$ direction, respectively. As shown in Fig. 3(a), the portion of the fatigue pre-crack (left of the figure) was smooth and uniform, while the 3D morphology of the intergranular crack was notably irregular; branching and discontinuous morphology. The existence of un-cracked ligaments (yellow arrows) can be clearly confirmed in the higher magnification image (Fig. 3(b)). This indicates that there were grain boundary plane segments that arrested crack propagation locally, resulting in a discontinuous crack morphology. The color in Fig. 3(c) expresses the thickness value (i.e., opening displacement) of the crack component according to the color bar presented below. The crack thickness basically decreased as approaching the crack tip. A certain crack-opening displacement suggests that the main fracture is mode I type. In general, normal stress resolved on the grain boundary plane significantly contributes to mode I fracture, i.e., higher resolved normal stress facilitates intergranular fracture. We chose four adjacent grain boundary cracks indicated in Fig. 3(c) (G.B.1, G.B.2, G.B.3, and G.B.4) to study the relationship between the resolved normal stress based on the remote

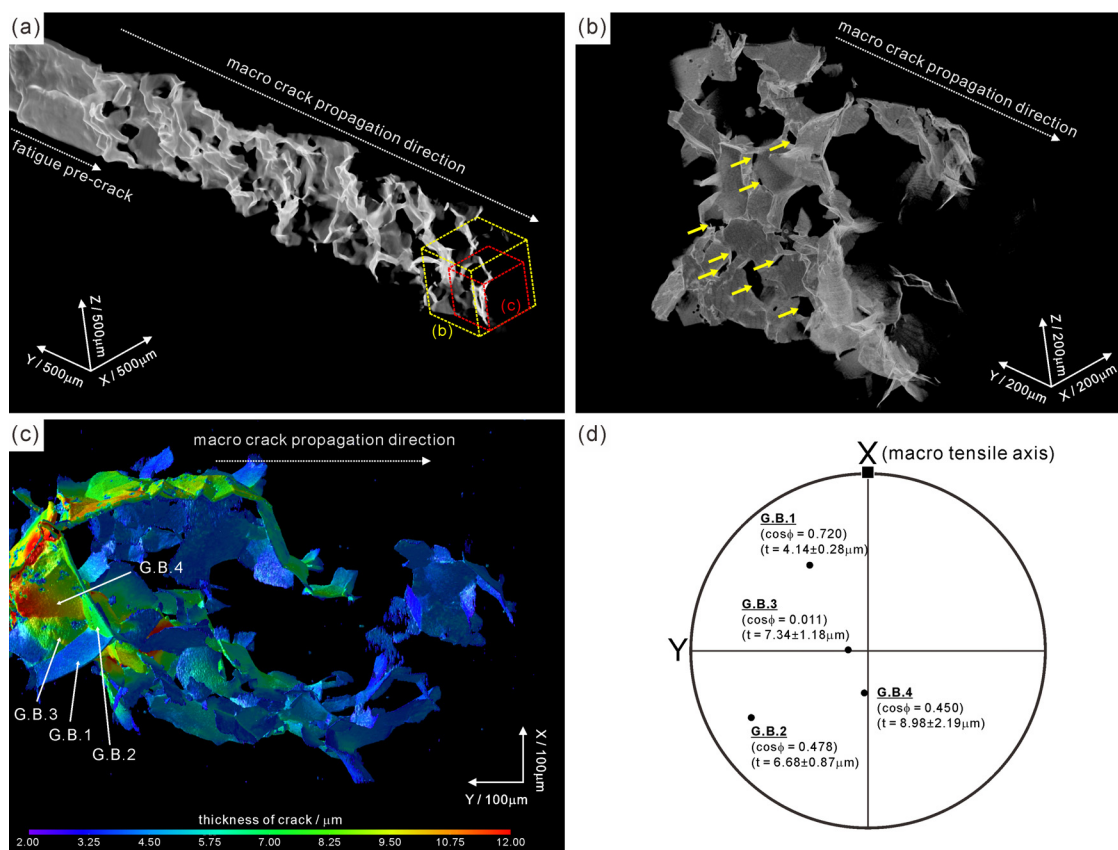


Fig. 3. 3D crack propagation morphology reconstructed by X-ray computed tomography; (a) the entire length of the crack, (b, c) the components around the macroscopic crack tip, and (d) stereographic projection showing the normal directions of the grain boundary cracks (G.B.) 1 ~ 4 in (c). The macroscopic directions of crack propagation and tensile axis were $-Y$ direction and $\pm X$ direction, respectively. The positions of the un-cracked ligaments are indicated by yellow arrows in (b). The color in (c) indicates the thickness of the crack component. Value of $\cos \phi$ (ϕ is the angle between the macroscopic tensile axis and normal direction of the grain boundary crack) and thicknesses of the four studied grain boundary cracks G.B.1 ~ 4 are listed in (d).

load and crack thickness (crack-opening displacement). The normal directions of the crack planes, that is, the grain boundary planes, are shown in the stereographic projection in Fig. 3(d). The angle between the macroscopic tensile axis ($\pm X$ direction) and grain boundary plane is defined as ϕ . The values of $\cos \phi$ and crack thickness (t) for each grain boundary crack plane are listed in Fig. 3(d): (G.B.1: $\cos \phi = 0.720$, $t = 4.14 \pm 0.28 \mu\text{m}$; G.B.2: $\cos \phi = 0.478$, $t = 6.68 \pm 0.87 \mu\text{m}$; G.B.3: $\cos \phi = 0.011$, $t = 7.34 \pm 1.18 \mu\text{m}$; G.B.4: $\cos \phi = 0.450$, $t = 8.98 \pm 2.19 \mu\text{m}$). A larger $\cos \phi$ value indicates larger resolved normal stress. The G.B.1 had the largest $\cos \phi$ value (0.720) and the smallest crack-opening displacement ($4.14 \pm 0.28 \mu\text{m}$) among the four adjacent grain boundaries. The G.B.3 exhibited the second largest crack-opening displacement ($7.34 \pm 1.18 \mu\text{m}$) in spite of its extremely small $\cos \phi$ value (0.011), i.e., small resolved normal stress. The results suggest that the crack-opening displacement was not simply related with the resolved normal stress. The analysis described above was based on the simple assumption using the remote load. The complicated stress field and/or plastic accommodation around the crack on a microscopic scale can have an influence on the crack-opening displacement. However, particularly, the microscopic stress field is difficult to evaluate experimentally. In the future, we aim to elucidate the crack propagation behavior by simulating microscopic stress field and plastic accommodation.

3.3. Microscopic 3D analysis of crack propagation

By analyzing 13 crack tips on the 2D section by SEM and EBSD, we found that the crack propagations were arrested at the

grain boundary triple junctions (i.e., grain boundary edges) or at the grain boundary planes. To understand the mechanism of local crack-arrestability (i.e., arrestability of individual cracks) from a crystallographic and microstructural point of view, the microscopic 3D crack propagation behaviors were investigated via FIB-SEM serial sectioning. The characteristic results are shown in Figs. 4, 5, and 6 where the crack propagation on the first observed sections ($Z = 0 \mu\text{m}$) was arrested at a portion of the grain boundary plane with crack-tip blunting (case 1, Fig. 4(a)), at the triple junction of the grain boundaries with crack-tip blunting (case 2, Fig. 5(a)), and at the triple junction of the grain boundaries without clear crack-tip blunting (case 3, Fig. 6(a)). The positions of the grain boundaries ahead of the cracks determined by EBSD orientation analysis are indicated by the white broken lines (in the following images, the white broken lines indicate the positions of the grain boundaries).

The 3D morphology of the crack that was arrested at the grain boundary plane was reconstructed from the SEM images of each section and is presented in Fig. 4(b). The color represents the thickness of the crack component. It was revealed that the blunting behavior was not uniform even at an identical crack: the tip was blunted at the depth of $Z = 0 \sim -3.8 \mu\text{m}$ (indicated by “blunting”), whereas the tip was rather sharp and not blunted at the depth of $Z < -3.9 \mu\text{m}$ (indicated by “no blunting”). A 3D EBSD orientation map around the crack is shown in Fig. 4(c). It is clear that the crack propagated in an intergranular manner on the grain boundary (prior austenite grain boundary). Fig. 4(d – i) shows the analysis results of two other representative sections: (d, g) SEM images, (e, h) 3D EBSD orientation maps, and (f, i) $\langle 001 \rangle$ pole fig-

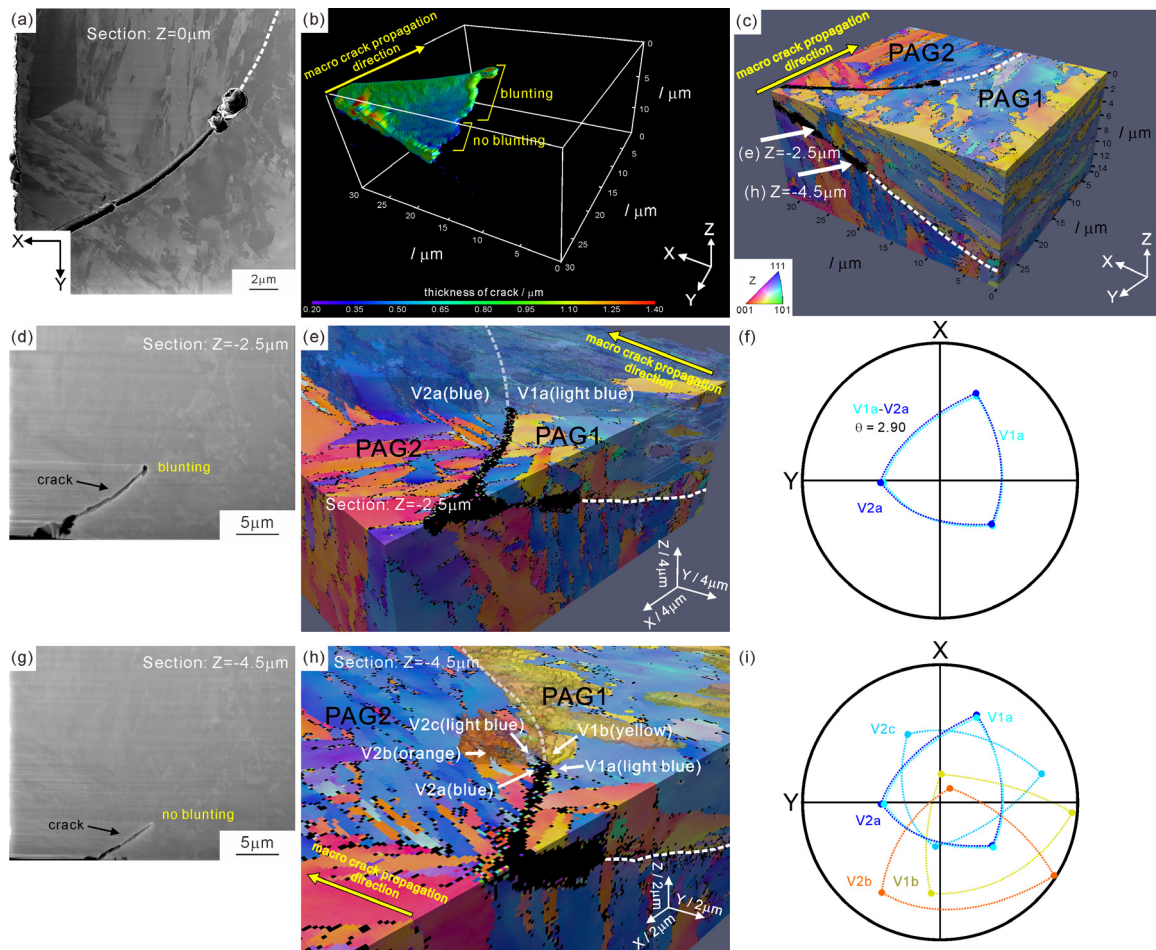


Fig. 4. Microscopic 3D crack propagation morphology reconstructed by FIB-SEM serial sectioning (case 1); (a) SEM image showing the first section ($Z = 0 \mu\text{m}$), (b) 3D crack morphology (the color indicates the thickness of the crack component), (c) 3D EBSD orientation map of the entire analyzed volume, and (d – i) SEM images (d, g), 3D EBSD orientation maps (e, h), and $\langle 001 \rangle$ pole figures showing the orientation of the martensite variants (f, i) at the top section $Z = -2.5 \mu\text{m}$ (d – f) and $-4.5 \mu\text{m}$ (g – i). In (e, h), the martensite variants existing ahead of the crack and above the top section are superimposed.

ures of the martensite variants existing around the crack tip. In the 3D EBSD orientation maps (Fig. 4(e, h)), the martensite variants existing ahead of the crack and above the corresponding section are superimposed. The variant number indicates the prior austenite grain where the variant existed (for example, V1 and V2 denote the variants that belong to the prior austenite grains of 1 and 2, respectively). At the section of $Z = -2.5 \mu\text{m}$, the crack tip was blunted (Fig. 4(d)) and the grain boundary plane segment ahead of the crack tip had a considerably small misorientation angle ($\theta = 2.9^\circ$) (Fig. 4(e, f)). Moreover, two relatively large martensite variants with small misorientation angle (V1a (light blue) and V2a (blue)) can be observed. In contrast, the crack tip at the section of $Z = -4.5 \mu\text{m}$ was rather sharp (Fig. 4(g)). Several small martensite variants with large misorientation angles were present around the crack tip (V1a (light blue), V1b (yellow), V2a (blue), V2b (orange), and V2c (light blue)) in Fig. 4(h, i). For example, the misorientation angle between V1b and V2c was 50.71° .

The crack shown in Fig. 5(a) propagated along the grain boundary 1 (G.B.1) and was arrested at the triple junction among G.B.1, G.B.2, and G.B.3 (close to the corner of G.B.1 ~ G.B.4). The grain boundaries in Fig. 5(b) were not flat and consisted of several segments. The orientations of the grain boundary plane segments with respect to the specimen coordinate are plotted on the stereographic projection shown in Fig. 5(c) along with the values of $\cos\phi$ for each grain boundary plane segment. The $\cos\phi$ values for the segments of G.B.1 on which the crack propagated were 0.494

(G.B.1-1) and 0.355 (G.B.1-2), much smaller than those for the segments of G.B.2-1 ($\cos\phi = 0.732$), G.B.2-2 ($\cos\phi = 0.997$), and G.B.3-1 ($\cos\phi = 0.762$). Although a large resolved normal stress was imposed on G.B.2 and G.B.3, the crack propagation was arrested at the grain boundary triple junction and did not propagate on those grain boundaries. The reconstructed 3D crack morphology is presented in Fig. 5(d), in which the color indicates crack thickness. As in the crack shown in Fig. 4, the blunting behavior was not uniform: blunted at $Z = 0 \sim -8.5 \mu\text{m}$, and not blunted at $Z < -8.5 \mu\text{m}$. In the depth range of 0 to $-8.5 \mu\text{m}$, relatively large martensite variants were confirmed in the region ahead of the grain boundary triple junction. Fig. 5(e, g) shows the representative cases and 3D EBSD orientation maps with top surfaces at $Z = -2.5 \mu\text{m}$ and $-8.9 \mu\text{m}$, respectively. At the $Z = -2.5 \mu\text{m}$ section (Fig. 5(e)), a relatively large martensite variant (V3a) can be observed around the grain boundary triple junction. In contrast, at the $Z = -8.9 \mu\text{m}$ section (Fig. 5(g)), several martensite variants (V3a, V3b, and V3c) can be observed around the grain boundary triple junction. These martensite variants had large misorientation with respect to one another as shown in Fig. 5(h).

Fig. 6(a, b) shows the crack that propagated along G.B.1 and was arrested at the triple junction among the G.B.1, G.B.2, and G.B.3. As shown in the stereographic projection in Fig. 6(c), the $\cos\phi$ value of G.B.2 was the largest (G.B.2-1: 0.580 and G.B.2-2: 0.685), while that of G.B.3 was almost zero (0.070). The fact that the crack did not propagate on G.B.3 is likely because of the small

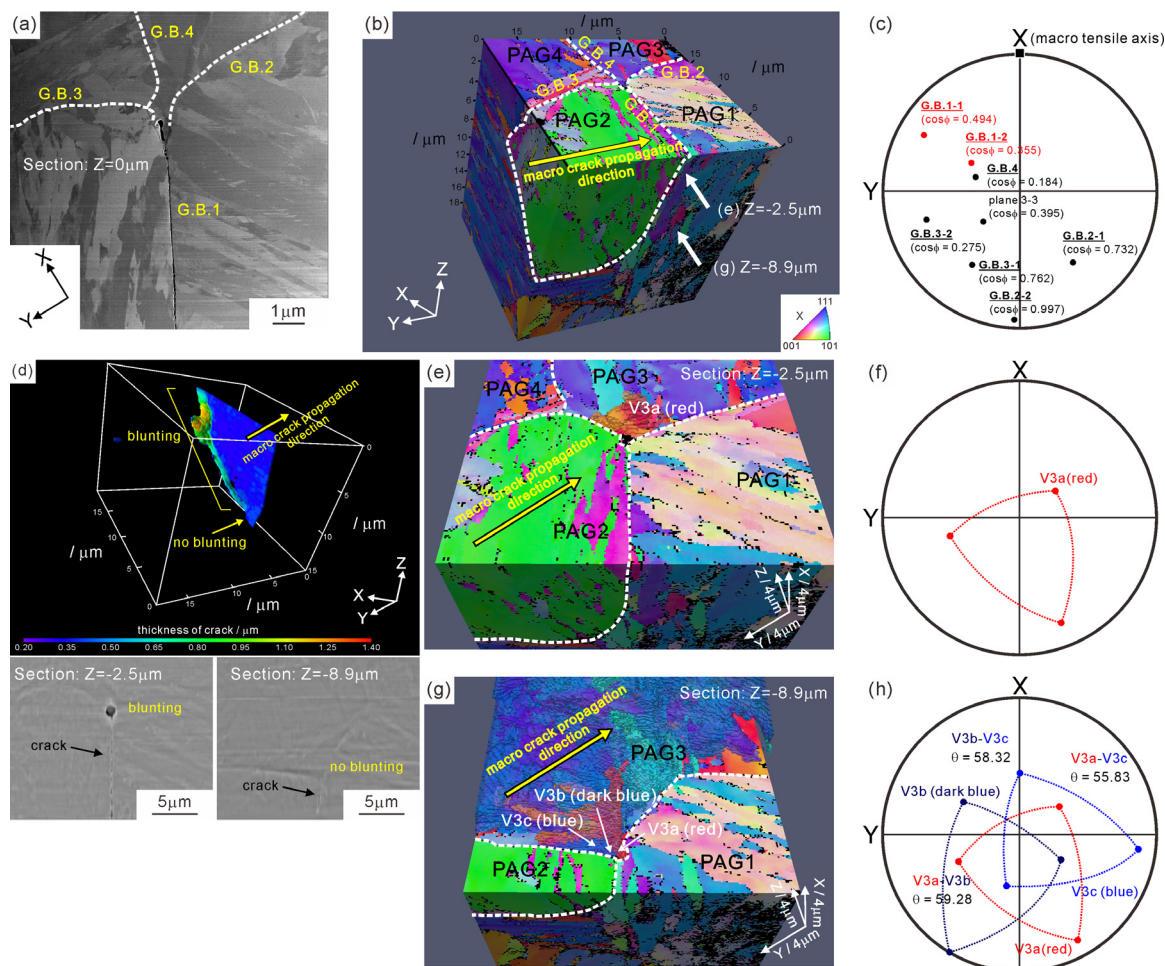


Fig. 5. Microscopic 3D crack propagation morphology reconstructed by FIB-SEM serial sectioning (case 2); (a) SEM image showing the first section ($Z = 0 \mu\text{m}$), (b) 3D EBSD orientation map of the entire analyzed volume, (c) stereographic projection showing the normal directions of the grain boundaries (G.B.) 1 ~ 4 (ϕ is the angle between the macroscopic tensile axis and normal direction of the G.B.), (d) 3D crack morphology (the color indicates the thickness of the crack component) and SEM images of the sections at $Z = -2.5 \mu\text{m}$ and $-8.9 \mu\text{m}$, and (e - h) 3D EBSD orientation maps (e, g) and $\langle -001 \rangle$ pole figures showing the orientation of martensite variants (f, h) at the top section $Z = -2.5 \mu\text{m}$ (e, f) and $-8.9 \mu\text{m}$ (g, h). In (e, g), the martensite variants existing ahead of the crack and above the top section are superimposed.

resolved normal stress. However, the crack did not propagate on G.B.2 even with its larger resolved normal stress compared to that on G.B.1. We confirmed that the tip of crack was sharp in the analyzed volume (Fig. 6(d)). Fig. 6(e, g) indicates that G.B.2 mainly corresponded to the boundary between the martensite variants of V1 and V2a, the misorientation angle between which was small ($\theta = 10.90^\circ$). Similar to the case shown in Fig. 4, G.B.2 acted as an obstacle to crack propagation due to the small misorientation. The relatively small martensite variant V2b existed around the grain boundary triple junction. Because the boundary between the martensite variants of V2a and V2b had a large misorientation angle of 59.82° (Fig. 6(f)), we infer that this high-angle boundary hindered the plastic accommodation of stress concentration and crack-tip blunting.

4. Discussion

The SEM image of the mid-thickness section (Fig. 2(d)) clearly suggests that the intergranular crack propagated in a discontinuous manner. However, it is difficult to deny the possibility that this behavior was limited only on the observed section. The results of the X-ray computed tomography (Fig. 3) conclusively demonstrated that the intergranular crack propagation was discontinuous, evidenced by the existence of a certain area of un-cracked ligaments. Despite the brittle intergranular fracture mode, the crack propaga-

tion was stable (Fig. 2(a, b)), which could be attributed to its discontinuous crack propagation. The dimples existing between the intergranular surface components (Fig. 2(c)) would correspond to the fracture of the un-cracked ligaments during the final rupture process. Moreover, the geometrical analysis results (Fig. 3(c, d)) indicate that the crack-opening displacement was not only related to the resolved normal stress. Accordingly, we propose that the geometrical characteristics, that is, grain boundary plane orientation with respect to remote load, is not the only factor determining the intergranular crack propagation path. As shown in Fig. 1, the prior austenite grain boundaries were inhomogeneous and consisted of boundary segments with different crystallographic features (the average grain boundary segment length in the present martensite structure was $1.53 \mu\text{m}$). The non-uniform segments in the grain boundaries of lath martensite could result in the discontinuous crack propagations.

As shown in Figs. 2, 4, and 5, some of the crack tips were blunted. According to Shih [43], J and crack-tip opening displacement (δ_t) have the following relationship;

$$\delta_t = d_n \times J / \sigma_Y \quad (1)$$

where d_n is a function strongly dependent on strain hardening coefficient, ranging typically from 0.2 to 0.7 for plane strain condition [43], and σ_Y is the average of 0.2% proof strength and tensile strength (1055 MPa in the present martensitic steel [36]). The

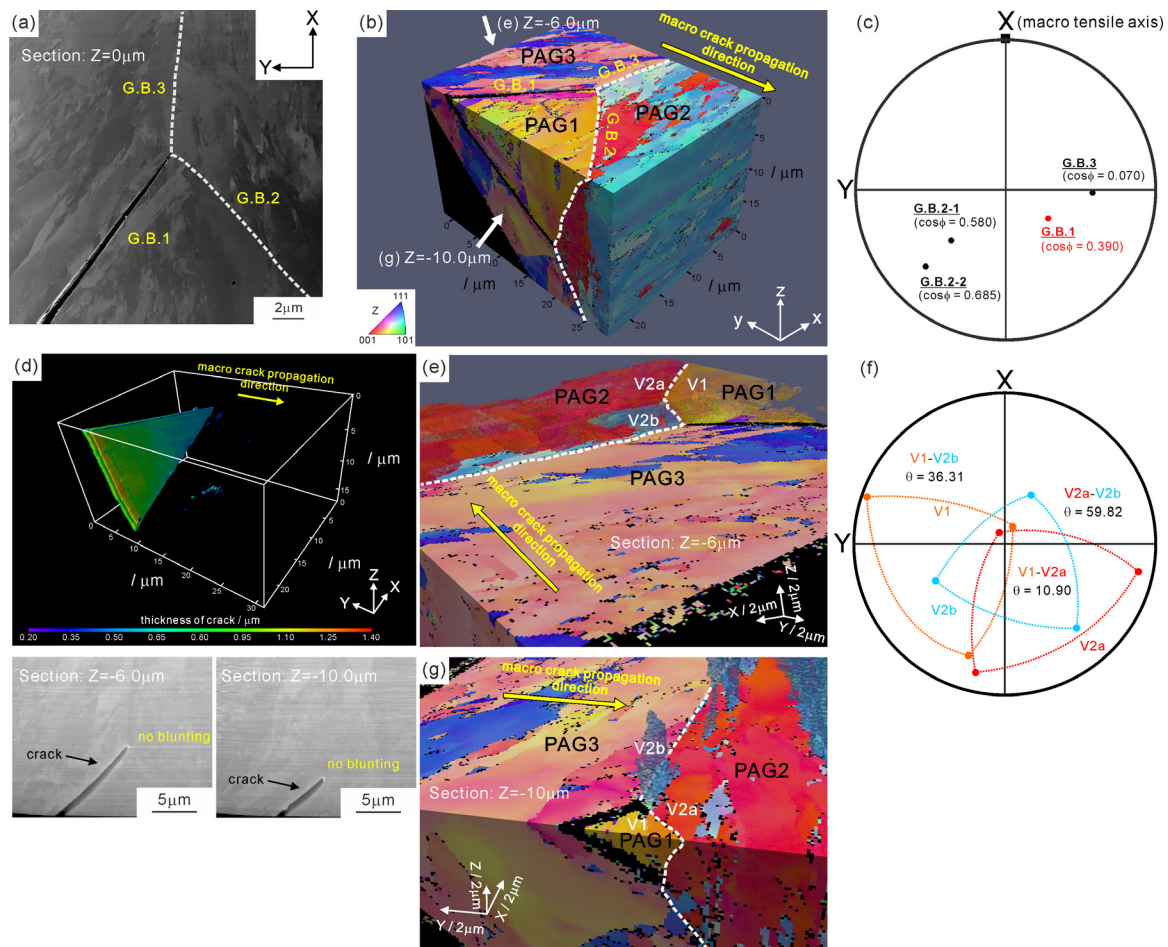


Fig. 6. Microscopic 3D crack propagation morphology reconstructed by FIB-SEM serial sectioning (case 3): (a) SEM image showing the first section ($Z = 0 \mu\text{m}$), (b) 3D EBSD orientation map of the entire analyzed volume, (c) stereographic projection showing the normal directions of the grain boundaries (G.B.) 1 ~ 3 (ϕ is the angle between the macroscopic tensile axis and normal direction of the grain boundary), (d) 3D crack morphology (the color indicates the thickness of the crack component) and SEM images of the sections at $Z = -6.0 \mu\text{m}$ and $-10.0 \mu\text{m}$, (e – g) 3D EBSD orientation maps (e, g), and $\langle 001 \rangle$ pole figures showing the orientation of martensite variants (f) at the top section $Z = -6.0 \mu\text{m}$ (e) and $-10.0 \mu\text{m}$ (g). In (e, g), the martensite variants existing ahead of the crack and above the top section are superimposed.

macroscopic J for the observed crack tips would be close to the fracture initiation toughness, J_{IC} (25.14 kJ m^{-2} [36]). The δ_t was estimated at $4.8 \sim 16.7 \mu\text{m}$ from Eq. 1, notably larger than the observed value (566 nm [42]). Typical fracture mechanics supposes that one main crack propagates continuously during fracture toughness test. However, the crack propagation behavior in the present study was discontinuous. This estimation suggests that the discontinuous crack propagation with un-cracked ligaments significantly affected the macroscopic mechanical properties, for example, toughening by crack bridging at the un-cracked ligament [44,45].

The FIB-SEM serial sectioning analysis results on three representative microscopic crack propagation behaviors (Figs. 4–6) revealed the following features: (i) there were several un-cracked grain boundary plane segments on which larger resolved normal stress was imposed than the cracked grain boundaries, (ii) crack propagation was arrested at the low-angle grain boundary plane segments and/or the grain boundary triple junctions surrounded by relatively large martensite variants, and (iii) crack-tip blunting was observed when larger martensite variants existed around the crack arrest sites. The microscopic analysis results also suggested that the resolved normal stress on the grain boundary was not the main factor contributing to intergranular crack propagation. We therefore deduced that atomistic decohesion at the low-angle grain boundaries was difficult to trigger, causing the arrest of

the intergranular crack propagation, as confirmed in Figs. 4 (d–f) and 6(e–g). Once the crack propagation was arrested, the blunting of the arrested crack tip occurred which was attributed to the accommodation of stress concentration by dislocation plasticity. Previous studies reported that the boundaries between martensite variants, specifically block boundaries and packet boundaries with large misorientation angles, could become obstacles to plastic deformation [46–48]. Therefore, the existence of large martensite variants promoted plastic accommodation, resulting in crack-tip blunting ($Z = 0 \sim -3.8 \mu\text{m}$ in Fig. 4 and $Z = 0 \sim -8.5 \mu\text{m}$ in Fig. 5). In contrast, plastic accommodation and crack-tip blunting were hindered by high-angle boundaries between martensite variants ($Z < -3.8 \mu\text{m}$ in Fig. 4, $Z < -8.5 \mu\text{m}$ in Fig. 5, and the entire volume of Fig. 6). Based on the above results, we propose that the low-angle grain boundary plane segment can act as an obstacle to intergranular crack propagation. The larger martensite variants around the grain boundary can promote plastic accommodation of stress concentration at the arrested crack tip, resulting in crack-tip blunting. Namely, the formation of un-cracked ligaments (observed in Fig. 3) is attributed to the low-angle grain boundary plane segments and the larger martensite variants existing around the grain boundary. The ductile fracture of the un-cracked ligaments contributes to the macroscopic resistance against crack propagation as reported previously [44,45,49–53]. The role of the misorientation angle of the grain boundary on intergranular crack propaga-

tion has been reported in both experimental and simulation works [3,5,54]. The present 3D analysis first confirmed this tendency in the intergranular crack on prior austenite grain boundaries in lath martensite structure, which exhibit a complicated structure compared with normal grain boundaries.

The findings described above are owing to the benefit of 3D analysis and difficult to obtain by conventional 2D analysis. Even when a crack arrest is confirmed on the observed section by 2D analysis, there is a large possibility that the critical reason for the crack arrest exists somewhat faraway above or below the observed section. For example, in the section of $Z = -4.5 \mu\text{m}$ shown in Fig. 4(h), the crack propagation was arrested at the boundary plane segment with a large misorientation (boundary between V1b and V2c, $\theta = 50.71^\circ$). However, the boundary plane segments with small misorientation angle existing in the region above the section of $Z = -3.8 \mu\text{m}$ could be attributed to the arrest of crack propagation, as shown in Fig. 4. Moreover, the characterization of the grain boundary plane orientation by 3D analysis leads to the important result that the geometrical condition of the grain boundary, that is, resolved normal stress, is not the main controlling factor, but the microstructural features (particularly, misorientation angle and existence of large martensite variants around prior austenite grain boundaries) are very important for intergranular crack propagation.

The results presented in this paper shed light on the concept of microstructure design for the enhancement of local crack-arrestability in high-strength martensitic steels. The martensite microstructure consisting of a large fraction of low-angle grain boundary plane segments as well as that of large martensite variants existing around the grain boundary could lead to high resistance to intergranular fracture. Increasing low-angle grain boundary plane segments can increase the chance to arrest crack propagation, because decohesion at low-angle grain boundaries is difficult to trigger [5]. Moreover, existence of large martensite variant can promote crack-tip blunting. Once the stress concentration around the crack tip is accommodated by dislocation plasticity, the resistance to further crack propagation increases and unstable premature fracture can be prevented. Finally, we propose that controlling the martensitic transformation, particularly variant selection at austenite grain boundaries in the nucleation stage, would be a possible method to obtain the optimal microstructure for enhancing local crack-arrestability and retarding intergranular fracture of high strength martensitic steels.

5. Conclusions

Through multi-scale 3D analysis utilizing X-ray computed tomography and FIB-SEM serial sectioning combined with 3D EBSD, we studied the intergranular crack propagation behavior in a high-strength martensitic steel. The major findings are summarized as follows:

1. The non-uniform 3D morphology of the intergranular crack and the presence of a certain area of un-cracked ligaments indicates that the crack propagated in a discontinuous manner. Considering the relationship between the geometrical characteristics and crack-opening displacement, we can conclude that the resolved normal stress imposed on the grain boundary plane is not the only factor determining the intergranular crack propagation path.
2. Through the microscopic 3D EBSD analysis of the three representative crack propagation behaviors, the following features were observed: (i) the resolved normal stress on the grain boundary is not the main factor controlling intergranular fracture, (ii) the low-angle grain boundary plane segment has a high local crack-arrestability and acts as an obstacle to crack propagation, and (iii) the existence of larger martensite vari-

ants enhances the plastic accommodation of stress concentration, resulting in crack-tip blunting.

3. Based on the obtained results, it can be considered that increasing the fraction of low-angle grain boundary plane segments can effectively enhance crack propagation arrestability, and that the existence of large martensite variants promotes plastic accommodation and resultant blunting of the arrested crack-tip. Therefore, we propose that a large fraction of low-angle grain boundary plane segments, as well as that of large martensite variants surrounding the grain boundaries is an optimal martensite microstructure for enhancing local crack-arrestability and retarding intergranular crack propagation.

Declaration of Competing Interest

The authors declare that they have no known competing financial interests or personal relationships that could have appeared to influence the work reported in this paper.

Acknowledgments

This study was financially supported by JST PRESTO (Grant Number JPMJPR2096), JSPS KAKENHI (Grant Numbers JP19H02459 and JP20K21083), and the Elements Strategy Initiative for Structural Materials (ESISM) through MEXT Japan. In addition, this study is based on results obtained from a project commissioned by the New Energy and Industrial Technology Development Organization (NEDO) [JPNP14014].

Supplementary materials

Supplementary material associated with this article can be found, in the online version, at doi:10.1016/j.actamat.2022.118053.

References

- [1] A. Pineau, A.A. Benzerga, T. Pardoen, Failure of metals I: Brittle and ductile fracture, *Acta Materialia* 107 (2016) 424–483.
- [2] T. Watanabe, Grain boundary engineering: historical perspective and future prospects, *Journal of Materials Science* 46 (2011) 4095–4115.
- [3] T. Watanabe, S. Turekawa, The control of brittleness and development of desirable mechanical properties in polycrystalline systems by grain boundary engineering, *Acta Materialia* 47 (1999) 4171–4185.
- [4] S. Bechtle, M. Kumar, B.P. Somerday, M.E. Launey, R.O. Ritchie, Grain-boundary engineering markedly reduces susceptibility to intergranular hydrogen embrittlement in metallic materials, *Acta Materialia* 57 (2009) 4148–4157.
- [5] D.V. Bachurin, Influence of grain boundary misorientation on intergranular fracture of nanocrystalline palladium, *International Journal of Fracture* 214 (2018) 69–78.
- [6] T. Hirano, Improvement of room temperature ductility of stoichiometric Ni3Al by unidirectional solidification, *Acta Metallurgica et Materialia* 38 (1990) 2667–2671.
- [7] D.C. Crawford, G.S. Was, The Role of grain boundary misorientation in intergranular cracking of Ni-16Cr-9Fe in 360°C argon and high-Purity water, *Metallurgical Transactions A* 23A (1992) 1195–1206.
- [8] P. Lin, G. Palumbo, U. Erb, K.T. Aust, Influence of grain boundary character distribution on sensitization and intergranular corrosion of alloy 600, *Scripta Metallurgica et Materialia* 33 (1995) 1387–1392.
- [9] S. Kobayashi, T. Maruyama, S. Tsurekawa, T. Watanabe, Grain boundary engineering based on fractal analysis for control of segregation-induced intergranular brittle fracture in polycrystalline nickel, *Acta Materialia* 60 (2012) 6200–6212.
- [10] I.M. Robertson, P. Sofronis, A. Nagao, M.L. Martin, S. Wang, D.W. Gross, K.E. Nygren, Hydrogen Embrittlement Understood, *Metallurgical and Materials Transactions B* 46B (2015) 1085–1103.
- [11] M. Dadfarnia, A. Nagao, S. Wang, M.L. Martin, B.P. Somerday, P. Sofronis, Recent advances on hydrogen embrittlement of structural materials, *International Journal of Fracture* 196 (2015) 223–243.
- [12] R.M. Horn, R.O. Ritchie, Mechanisms of tempered martensite embrittlement in low alloy steels, *Metallurgical Transaction A* 9A (1978) 1039–1053.
- [13] J. Kameda, C.J. McMahon Jr, Solute segregation and hydrogen-induced intergranular fracture in an alloy steel, *Metallurgical Transaction A* 14A (1983) 903–911.
- [14] A.R. Marder, G. Krauss, The morphology of martensite in iron-carbon alloys, *Transactions ASM* 60 (1967) 651–660.

- [15] J.M. Marder, A.R. Marder, The morphology of iron-nickel massive martensite, *Transactions ASM* 62 (1969) 1–10.
- [16] S. Morito, H. Tanaka, R. Konishi, T. Furuhashi, T. Maki, The morphology and crystallography of lath martensite in Fe-C alloys, *Acta Materialia* 51 (2003) 1789–1799.
- [17] S. Morito, X. Huang, T. Furuhashi, T. Maki, N. Hansen, The morphology and crystallography of lath martensite in alloy steels, *Acta Materialia* 54 (2006) 5323–5331.
- [18] S. Morito, J. Nishikawa, T. Maki, Dislocation Density within Lath Martensite in Fe-C and Fe-Ni alloys, *ISIJ International* 43 (2003) 1475–1477.
- [19] G. Krauss, Martensite in steel: strength and structure, *Materials Science and Engineering A* 273–275 (1999) 40–57.
- [20] A. Nagao, C.D. Smith, M. Dadfarnia, P. Sofronis, I.M. Robertson, The role of hydrogen in hydrogen embrittlement fracture of lath martensitic steel, *Acta Materialia* 60 (2012) 5182–5189.
- [21] S. Ueki, T. Matsumura, Y. Mine, S. Morito, K. Takashima, Microstructural fatigue crack growth in single-packet structures of ultra-low carbon steel lath martensite, *Scripta Materialia* 173 (2019) 80–85.
- [22] K. Okada, A. Shibata, Y. Takeda, N. Tsuji, Crystallographic analysis of fatigue fracture initiation in 8Ni-0.1C martensitic steel, *International Journal of Fatigue* 143 (2021) 105921.
- [23] L. Cho, P.E. Bradley, D.S. Lauria, M.L. Martin, M.J. Connolly, J.T. Benzing, E.J. Seo, K.O. Findley, J.G. Speer, A.J. Slifka, Characteristics and mechanisms of hydrogen-induced quasi-cleavage fracture of lath martensitic steel, *Acta Materialia* 206 (2021) 116635.
- [24] M. Ueda, H.Y. Yasuda, Y. Umakoshi, Effect of grain boundary character on the martensitic transformation in Fe–32at.%Ni bicrystals, *Acta Materialia* 49 (2001) 3421–3432.
- [25] M. Ueda, H.Y. Yasuda, Y. Umakoshi, Stress-induced martensitic transformation in Fe–Ni bicrystals, *Acta Materialia* 49 (2001) 4251–4258.
- [26] M. Ueda, H.Y. Yasuda, Y. Umakoshi, Controlling factor for nucleation of martensite at grain boundary in Fe–Ni bicrystals, *Acta Materialia* 51 (2003) 1007–1017.
- [27] T.F. Morgener, M.J. Starink, I. Sinclair, Evolution of voids during ductile crack propagation in an aluminium alloy sheet toughness test studied by synchrotron radiation computed tomography, *Acta Materialia* 56 (2008) 1671–1679.
- [28] S.P. Knight, M. Salazar, A.R. Trueman, The study of intergranular corrosion in aircraft aluminium alloys using X-ray tomography, *Corrosion Science* 53 (2011) 727–734.
- [29] H. Toda, E. Maire, S. Yamauchi, H. Tsuruta, T. Hiramatsu, M. Kobayashi, In situ observation of ductile fracture using X-ray tomography technique, *Acta Materialia* 59 (2011) 1995–2008.
- [30] H. Toda, A. Takijiri, M. Azuma, S. Yabu, K. Hayashi, D. Seo, M. Kobayashi, K. Hirayama, A. Takeuchi, K. Uesugi, Damage micromechanisms in dual-phase steel investigated with combined phase- and absorption-contrast tomography, *Acta Materialia* 126 (2017) 401–412.
- [31] H. Lamei Ramandi, H. Chen, A. Crosky, S. Saydam, Interactions of stress corrosion cracks in cold drawn pearlitic steel wires: An X-ray micro-computed tomography study, *Corrosion Science* 145 (2018) 170–179.
- [32] D.J. Rowenhorst, A. Gupta, C.R. Feng, G. Spanos, 3D Crystallographic and morphological analysis of coarse martensite: Combining EBSD and serial sectioning, *Scripta Materialia* 55 (2006) 11–16.
- [33] S. Zaeferrer, S.I. Wright, Three-Dimensional Orientation Microscopy by Serial Sectioning and EBSD-Based Orientation Mapping in a FIB-SEM, in: A. Schwartz, M. Kumar, B. Adams, D. Field (Eds.), *Electron Backscatter Diffraction in Materials Science*, Springer, Boston, MA, 2009, pp. 109–122.
- [34] S. Morito, Y. Edamatsu, K. Ichinotani, T. Ohba, T. Hayashi, Y. Adachi, T. Furuhashi, G. Miyamoto, N. Takayama, Quantitative analysis of three-dimensional morphology of martensite packets and blocks in iron-carbon-manganese steels, *Journal of Alloys and Compounds* 577 (2013) S587–S592.
- [35] S. Morito, A. Hoang Pham, T. Ohba, T. Hayashi, T. Furuhashi, G. Miyamoto, Three-dimensional observations of morphology of low-angle boundaries in ultra-low carbon lath martensite, *Microscopy* 66 (2017) 380–387.
- [36] A. Shibata, Y. Madi, K. Okada, N. Tsuji, J. Besson, Mechanical and microstructural analysis on hydrogen-related fracture in a martensitic steel, *International Journal of Hydrogen Energy* 44 (2019) 29034–29046.
- [37] ASTM E1820-17 Standard Test Method for Measurement of Fracture Toughness, 2017.
- [38] T. Hara, K. Tsuchiya, K. Tsuzaki, X. Man, T. Asahata, A. Uemoto, Application of orthogonally arranged FIB-SEM for precise microstructure analysis of materials, *Journal of Alloys and Compounds* 577 (2013) S717–S721.
- [39] Y. Bhandari, S. Sarkar, M. Groeber, M.D. Uchic, D.M. Dimiduk, S. Ghosh, 3D polycrystalline microstructure reconstruction from FIB generated serial sections for FE analysis, *Computational Materials Science* 41 (2007) 222–235.
- [40] J.K. Mackenzie, Second paper on statistics associated with the random disorientation of cubes, *Biometrika* 45 (1958) 229–240.
- [41] K. Chan, A new criterion for brittle-to-ductile fracture transition, *Acta Metallurgica* 37 (1989) 1217–1226.
- [42] A. Shibata, I. Gutierrez-Urrutia, K. Okada, G. Miyamoto, Y. Madi, J. Besson, K. Tsuzaki, Relationship between mechanical response and microscopic crack propagation behavior of hydrogen-related intergranular fracture in as-quenched martensitic steel, *Materials Science and Engineering A* 831 (2022) 142288.
- [43] C.F. Shih, Relationships between the J-integral and the crack opening displacement for stationary and extending cracks, *Journal of the Mechanics and Physics of Solids* 29 (1981) 305–326.
- [44] A.R. Rosenfield, B.S. Majumdar, Micromechanisms and toughness for cleavage fracture of steel, *Nuclear Engineering and Design* 105 (1987) 51–57.
- [45] M.Y. He, D.J. Wisnuchek, A.G. Evans, Toughening and strengthening by inclined ligament bridging, *Acta Materialia* 45 (1997) 2813–2820.
- [46] S. Morito, H. Yoshida, T. Maki, X. Huang, Effect of block size on the strength of lath martensite in low carbon steels, *Materials Science and Engineering A* 438–440 (2006) 237–240.
- [47] A. Shibata, T. Nagoshi, M. Sone, S. Morito, Y. Higo, Evaluation of the block boundary and sub-block boundary strengths of ferrous lath martensite using a micro-bending test, *Materials Science and Engineering A* 527 (2010) 7538–7544.
- [48] A. Shibata, T. Nagoshi, M. Sone, Y. Higo, Micromechanical characterization of deformation behavior in ferrous lath martensite, *Journal of Alloys and Compounds* 577 (2013) S555–S558.
- [49] R.G. Hoagland, A.R. Rosenfield, G.T. Hahn, Mechanisms of fast fracture and arrest in steels, *Metallurgical Transactions* 3 (1972) 123–136.
- [50] T. Lung, A. Pineau, Dynamic crack propagation and crack arrest investigated with a new specimen geometry: Part II: experimental study on a low-alloy ferritic steel, *Fatigue & Fracture of Engineering Materials & Structures* 19 (1996) 1369–1381.
- [51] F. Yanagimoto, T. Hemmi, Y. Suzuki, Y. Takashima, T. Kawabata, K. Shibamura, Contribution of grain size to resistance against cleavage crack propagation in ferritic steel, *Acta Materialia* 177 (2019) 96–106.
- [52] Y. Takashima, T. Kawabata, R. Deguchi, S. Yamada, F. Minami, Increase in micro-cracks beneath cleavage fracture surface in carbon steel ESSO specimens, *Theoretical and Applied Fracture Mechanics* 101 (2019) 365–372.
- [53] T. Kawabata, F. Tonsho, Y. Nishizono, N. Nakamura, Y. Takashima, Controlling factors for roughness increases on cleavage fracture surfaces and crack branching in polycrystalline steel, *Theoretical and Applied Fracture Mechanics* 100 (2019) 171–180.
- [54] B.B. Rath, I.M. Bernstein, The relation between grain-boundary orientation and intergranular cracking, *Metallurgical Transactions* 2 (1971) 2845–2851.